The final version of this paper was published in the proceedings of the conference as paper No. 2024-3157. https://doi.org/10.2514/6.2024-3157

Inflow distortion noise and turbulence measurements in a low speed fan test rig

Lukas Klähn*, Robert Meyer†, and Ulf Tapken‡
German Aerospace Center (DLR), Institute of Propulsion Technology, Berlin, Germany

In the context of emerging aircraft with boundary layer ingestion and high bypass ratios, fan broadband noise is expected to increase. On the one hand, broadband noise is excited when the ingested turbulence interacts with the rotor. On the other hand the distorted mean flow in the inlet affects the turbulence generated by the rotor, i.e. the rotor wakes and the tip vortex. In this study turbulence measurements upstream and downstream of the rotor with hot wires are combined with an in-duct sound power measurement technique in a laboratory fan test bench. The sound power is calculated based on a broadband radial mode analysis. Based on the increased turbulence measured downstream of the rotor, the rotor stator interaction is expected to increase with inflow distortion. The sound power measurements do not confirm this expectation. The reason for this contradiction are discussed in the paper. It is assumed that the rotor stator interaction noise is masked by the turbulence rotor interaction noise at high frequencies and possibly by low frequency stall noise that arises when the rotor blade passes through the inflow distortion. These assessments are supported by the hot wire measurements.

List of Symbols

Latin Symbols

$A^{\pm}_{mn}$	amplitude of acoustic mode in Pa
B	blade number
c	speed of sound in m/s
f	frequency
f_{rot}	rotor shaft frequency
f_{mn}	radial mode shape function
H_{12}	shape factor
$k^{\pm}_{mn}$	axial wave number of acoustic mode in 1/m
$\dot{m}_c$	corrected mass flow
M_x	axial Mach number
$p(\boldsymbol{x})$	sound pressure Pa at position $\boldsymbol{x}$
$\tilde{r}$	scaled radius
R	duct radius in m
R_h	hub radius
S_{uu}, S_{vv}	velocity power spectral density
$\boldsymbol{S}_{p_o p_l(x_j)}$	cross spectral densities between the ring array and the sensor at position x_j in the line array.
T_u, T_v, T_w	axial, radial and circumferential component of turbulence intensity

*Research Associate, Engine Acoustics Department, Bismarckstr. 101, 10625 Berlin, Lukas.Klaehn@dlr.de.
†Research Scientist, Engine Acoustics Department, Bismarckstr. 101, 10625 Berlin, Robert.Meyer@dlr.de.
‡Research Scientist, Engine Acoustics Department, Bismarckstr. 101, 10625 Berlin, Ulf.Tapken@dlr.de.

$\tilde{\boldsymbol{u}}^2$	$= [\tilde{u}^2, \tilde{v}^2, \tilde{w}^2]$, variance of fluctuating velocity vector
$\boldsymbol{U}$	$= [U, V, W]$, mean velocity vector
$\boldsymbol{u}$	$= [u, v, w]$, velocity vector
$\boldsymbol{u'}$	$= [u', v', w']$, fluctuating velocity vector
U_∞	free flow velocity
U_{tip}	rotor tip velocity
$\dot{V}$	volume flow
$\boldsymbol{x}$	$= [x, r, \theta]$, axial, radial and circumferential coordinate

Greek symbols

α_{mn}	propagation factor of acoustic mode
δ_1	displacement thickness
δ_2	momentum thickness
δ_{99}	boundary layer thickness
Λ	turbulence length scale
Π_p	fan pressure ratio
ρ	density in kg/m^3
σ_{mn}	eigenvalue
Φ	flow coefficient

Acronyms

BLI	boundary layer ingestion
BPF	blade passing frequency
CRAFT	co-/ contra rotating acoustic fan test
HW1, HW2	hot wire probes of type 1 and 2, respectively
RPM	revolutions per minute
RSI	rotor stator interaction
TKE	turbulence kinetic energy
TRI	turbulence rotor interaction

Subscripts

$()_x$, $()_r$, $()_\theta$	axial, radial and circumferential component

I. Introduction

The increased sound excitation of fans due to disturbed inflow must be given high attention, as this is associated with future installed flight propulsion systems, such as engine embedding to utilize boundary layer suction. Boundary layer ingestion (BLI) has the potential to reduce the fuel consumption of emerging aircraft [1, 2]. Hence, BLI may be a feasible approach to achieve the ambitious goals of the European commission's FLIGTHPATH-2050 [3]. Besides the substantial reduction of greenhouse gas emissions, the commission also sets ambitious goals to reduce the noise emissions of flying aircraft. Thus, reliable fan noise prediction is essential in early design stages of future aircraft with integrated engines. These predictions require a detailed comprehension of the correlations between the disturbed inflow an the fan noise sources. The current study supports this goal.

The inflow of a turbofan with BLI can be characterized by a thick turbulent boundary layer in one segment of the duct with a spatially non-homogeneous total pressure loss. The related profile of the average velocity and increased turbulent kinetic energy have a substantial effect on the fan acoustics. The focus of this study is on the broadband noise, although tonal noise sources are influenced by BLI as well [4–6].

Under clean inflow conditions, the rotor-stator interaction (RSI) noise is typically the strongest fan noise source. This noise source is in modern fan designs mainly excited by unsteady loading on the stator vanes due to the rotor wakes [7]. As the turbulent length scales are limited by the wakes dimensions, no blade to blade correlations occur. Guérin et al. [8], Lewis et al. [9] model this noise source with a hybrid approach: Based on a CFD calculation of the rotor wakes, the acoustic sources are calculated with analytical models. Similarly, hot wire measurements can be used to measure the wake properties. Then, the same models can be used as if the wake properties were extracted from CFD calculations.

When the fan is ingesting a boundary layer, or a different inflow distortion, the non-homogeneous average velocity at the fan face leads to locally non-ideal blade incidence flow angles, and subsequently to a modulation of the rotor wakes. As the rotor blades are locally exposed to higher loading, the boundary layer thickness on the blade suction side is increased or the flow may even stall. Consequently the turbulent kinetic energy impinging on the stator vanes is increased. As a result, we expect an increase in the broadband RSI noise [10].

Not only the RSI noise is affected by the inflow distortion, but also an additional noise source is excited. When exposed to BLI, the interaction between the distorted turbulent inflow and the rotor blades leads to fan noise excitation. This turbulence-rotor interaction (TRI) noise source is excited by the inflow turbulence that causes random lift force fluctuations on the rotor blades [11, 12]. However, the physical mechanisms of broadband TRI and tonal inflow-rotor interaction noise are identical [13]. Therefore, analytical models of this noise source include the description of variable blade to blade correlations. The two extremes are either fully correlated blade forces, where the model represents a tonal noise source, or fully uncorrelated blade forces, where the noise source is purely broadband. Between those two extremes are continuous solutions with different degrees of blade to blade correlations that can lead to haystacks at the blade passing frequency (BPF) and its harmonics [11–17].

In this context Caldas et al. [18] and Klähn et al. [10] investigated inflow distortions, similar to BLI, by means of acoustic and aerodynamic measurements in a laboratory fan test rig i.e. the Co-/Contra Rotating Acoustic Fan Test rig (CRAFT) [19]. Perforated plates, mounted on a flow straightener, were used to vary the mean flow and the turbulence properties [18]. The acoustic excitation was measured with microphone arrays in the duct up- and downstream of the fan [6, 10]. The method the authors used to create the inflow distortion profile prevented larger turbulent structures and blade to blade correlations to emerge. Furthermore, the created flow profile resembled a smoothed step function and was more of theoretical interest. While in these experiments multiple academic distortion profiles were examined, in the current study the aim was to create a realistic BLI profile. A more realistic inflow distortion was designed by Kajasa et al. [20], who designed a distortion fence with the help of CFD calculations. Their distortion fence recreated a BLI profile from a CFD simulation of a full airplane. Lengyel-Kampmann et al. [21] and Meyer et al. [22] used this fence to measure the influence of BLI on the aerodynamics and acoustics of a counter-rotating fan in a large scale test rig with representative Mach numbers. We used the same distortion fence design, in a scaled version, to create a more realistic mean flow profile. The measurements of the average and turbulent flow conditions up and downstream of the rotor as well as acoustic in-duct measurements upstream of the fan are presented in this work.

The aim is to experimentally determine the relationships between the disturbed inflow, the disturbed rotor wakes and the modification of the broadband fan noise sources. For this purpose, the turbulence and average velocities were measured with and without inflow distortion up- and downstream of the rotor with hot wires [23, 24]. The broadband noise was measured with flush mounted microphones in the inlet section. The microphones are arranged as a combined axial and azimuthal sensor array [25]. This should improve the basic understanding and provide verification data for modeling methods to predict the impact of inflow distortions on the broadband fan noise.

The Structure of the paper is the following. In section II the CRAFT test rig and the inflow distortion are described. In section III the methods to determine the average flow and turbulence properties from the hot wire measurements are summarized. Furthermore, in section IV the sound power calculations from the in duct microphone measurements are summarized. Then, in section V not only the measurements of average flow and turbulence properties upstream of the fan and downstream of the rotor are shown, but also the determined broadband noise sound power levels are presented. Finally, in section VII we discuss and summarize the results.

II. Description of the Co-/ Contra Rotating Acoustic Fan Test rig (CRAFT)

The experiments were conducted at the CRAFT rig, a low speed acoustic fan test rig with a diameter of 453.6 mm. The used reference fan consists of 18 rotor blades and 21 stator vanes. The rotor speed is 4500 rpm at the design operating point resulting in a mass flow of 6.9 kg/s.

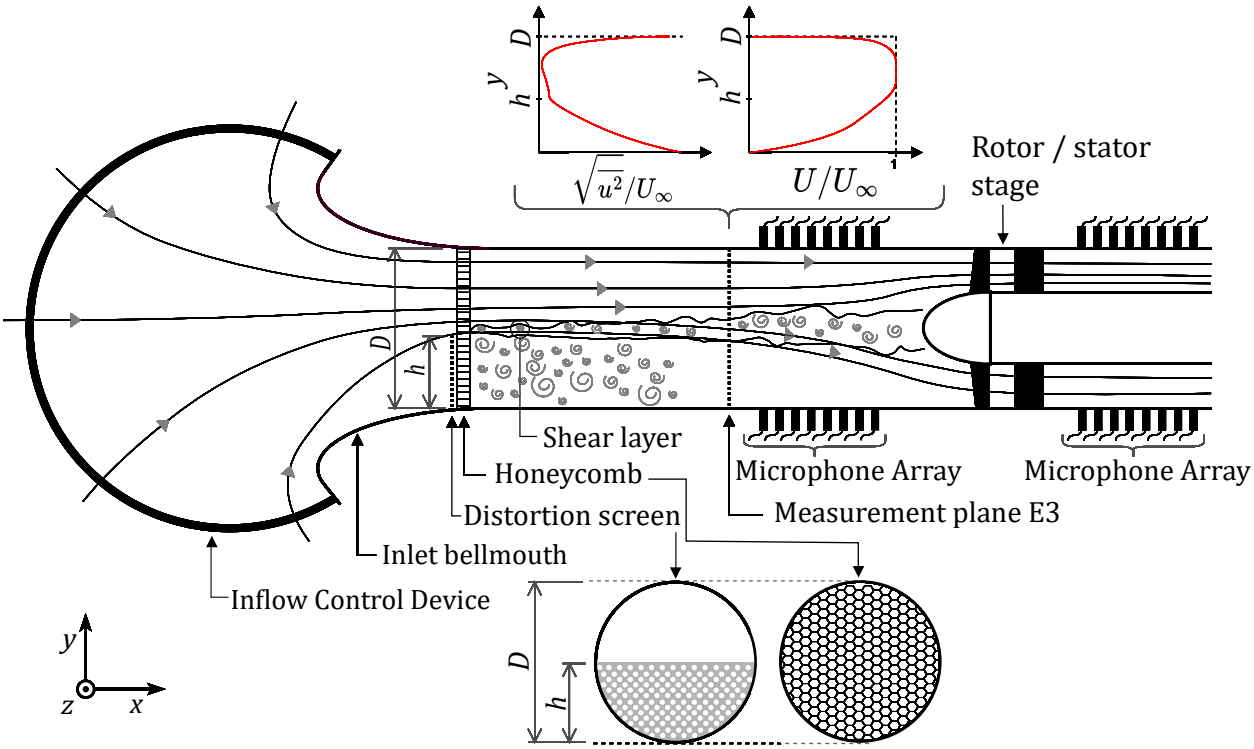

Figure 1 Sketch of the measurement setup of the CRAFT rig. The distortion screen is replaced with the one shown in Fig. 3 right with an increased distance to the honeycomb.

A sketch of the experimental setup is depicted in Fig. 1. Following the stream lines from left to right, the flow is first conditioned by an inflow control device (Fig. 2, left) that ensures a consistent turbulence distribution of low intensity and small length scales upstream of the bell mouth inlet [26]. Downstream of the bell mouth a device for the controlled generation of inflow distortions can be installed. In the current study it consists of a distortion fence, which is inserted 140 mm into the duct (the design of the studied distortion fence differs from the sketch in Fig. 1, see right of Fig. 3). The mass flow is determined with static pressure holes and a Pitot tube between the distortion device and the bell mouth inlet. 75 mm downstream of the distortion a flow straightener is mounted. The reason are two counter-rotating eddies that arise from the edges of the fence and are smoothed out by the honeycomb. The acoustic and aerodynamic instrumentation is located between the honeycomb and the rotor (see also Fig. 2, right). Behind the stator the outlet measurement section is located, followed by the primary structures of the test bench and a throttling device, not shown in Fig. 1. A detailed description of the test rig is given by Tapken et al. [19].

A. Inflow distortion screen design

In Fig. 3 the clean configuration and the inflow distortion fence are depicted. Left a picture of the flow straightener mounted in the inlet is shown. The rotor casing is open in this picture, hence the rotor is illuminated in the duct.

The distortion on the right is based on a design by Kajasa et al. [20]. The authors used experimental studies and numerical simulations to design a distortion fence that is able to reproduce the inflow conditions of a boundary layer ingesting engine embedded into the fuselage of a mid-range civil aircraft [27]. Lengyel-Kampmann et al. [21] successfully used the design in full scale experiments at the multistage two shaft compressor test facility (M2VP). Meyer et al. [22] describe the turbulence and aeroacoustic measurements of these tests. In the large scale tests with a diameter of 1 m, the

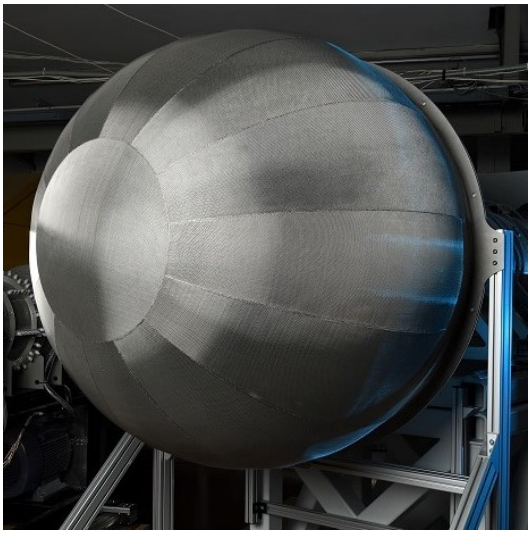

Figure 2 (left) inflow control device; (right) front view of the fan with aerodynamic measurement probes installed

Figure 3 Tested inlet configurations: (left) flow straightener as clean configuration; (right) distortion fence designed for reproduction of a realistic BLI profile

fence was not inserted more than 120 mm into the inlet (12.6 % of the duct diameter), to avoid severe blade vibrations. In the experimental setup at the CRAFT rig, the fence is inserted 140 mm (30.9 % of the duct diameter) and hence the distortion affects a much bigger portion of the cross sectional area. Based on the setup in the large scale experiments, the distortion fence is mounted 75 mm upstream of the flow straightener.

B. Measured operating conditions

The measurements are performed at three operating conditions at the maximum rotation speed of 4500 rpm. The mass flow and rotation speed were normalized with respect to the standard atmospheric conditions at sea level, i. e. $T_{\text{ref}} = 288.15\,\text{K}$ and $p_{\text{ref}} = 101\,325\,\text{Pa}$ to assure Mach number similarity between measurements. The three operating conditions are named *high loading*, *working line* and *high mass flow* in this paper. The operating points have the same maximum rotation speed of 4500 rpm but differ in their mass flow $\dot{m}$ and fan pressure ratio Π_p. In section V the

operating points are labeled by means of the flow coefficient Φ:

$$\Phi = \frac{\dot{V}}{\pi R^2 U_{\text{tip}}} = \frac{M_x}{M_{\text{tip}}}, \tag{1}$$

with $\dot{V}$ the volume flow, and U_{tip} the rotor tip velocity. The specifications of the operating points are summarized in table 1.

Table 1 Names, flow coefficients, corrected mass flows, axial Mach numbers and fan pressure ratios for the three operating points in the clean configuration.

	Φ	$\dot{m}_c$ in kg/s	M_x	Π_p
high loading	0.28	5.9	0.09	1.043
working line	0.33	7.0	0.10	1.038
high mass flow	0.40	8.5	0.13	1.029

In the configuration with inflow distortion, the mass flow is measured upstream of the distortion fence. Therefore, the flow coefficient, the mass flow and the rotation speed are the same for the clean and the distorted case. while the fan pressure ratio and is expected to be smaller with the inflow distortion. The Mach number is equivalent upstream of the distortion fence and may differ downstream of it because of the pressure drop that is induced by the fence.

III. Aerodynamic measurements with hot wire anemometry up- and downstream of the rotor

A. Turbulence measurements in the inlet section

Aerodynamic measurements of the inflow conditions are performed by means of hot-wire anemometers 670 mm upstream of the rotor leading edge in plane E3, see Fig. 1. The hot wire measurements in the inlet are performed with two x-wire probes at 30 radial positions. The first hot wire probe (HW1) is used to measure the axial and the radial components of the turbulent velocities u' and v', whereas the second probe (HW2) is used to measure the axial and the tangential components of the turbulent velocities u' and w'. The two hot wire probes are staggered azimuthally with an angle of 17.1°. The hot wire probes are calibrated by evaluating the Reynolds and Nusselt numbers. As described by Meyer et al. [24], this procedure reduces the influence of Mach number, Temperature and static pressure on the measurements. For further details on the measurement procedure the reader is referred to [23].

To calculate the turbulence properties, the velocity Vector is divided into an average and a fluctuating component:

$$\boldsymbol{u}(\boldsymbol{x}, t) = \boldsymbol{U}(\boldsymbol{x}, t) + \boldsymbol{u'}(\boldsymbol{x}, t) \ . \tag{2}$$

From the fluctuating component $\boldsymbol{u'}$ the the auto power spectral density (PSD) S is calculated via fast fourier transform (FFT). The variance of the velocity fluctuations is obtained from the auto PSD. For the auto PSD of the axial velocity component S_{uu} the variance $\tilde{u}^2$ is calculated as:

$$\tilde{u}^2 = \int_{-\infty}^{\infty} S_{uu}(f) df \ , \tag{3}$$

for the radial component $\tilde{v}^2$ and the circumferential component $\tilde{w}^2$ analogous. The root mean square of the the velocity is:

$$u_{\text{rms}} = \sqrt{\tilde{u}^2} \tag{4}$$

The turbulence intensity is the ratio of the variance of the fluctuating velocity and the average velocity. For the axial component that is:

$$T_u = \frac{u_{\text{rms}}}{U} \ . \tag{5}$$

Note, that we use the local average velocity to define the turbulence intensity. The turbulence kinetic energy is the half sum of the variances:

$$\mathrm{TKE} = \frac{1}{2}(\tilde{u}^2 + \tilde{v}^2 + \tilde{w}^2)\,. \tag{6}$$

The three dimensional variance can be determined by combinig the two X-wire probes. In this work however, the TKE is calculated by assuming an axisymmetric turbulence. For example for HW1:

$$\mathrm{TKE} = \frac{1}{2}(\tilde{u}^2 + 2\tilde{v}^2)\,. \tag{7}$$

The calculation of turbulent length scales is based on a hypothesis of homogeneous and isotropic turbulence. As described in detail by [28], the turbulent length scales Λ can be estimated as:

$$\Lambda_u = \lim_{f\to 0} \frac{S_{uu}(f)U}{4\tilde{u}^2}\,, \tag{8}$$

$$\Lambda_v = \lim_{f\to 0} \frac{S_{vv}(f)U}{2\tilde{v}^2}\,. \tag{9}$$

Here the subscripts u and v denote the axial and radial component of the turbulence and S_{uu} and S_{vv} are the power spectral densities of the respective velocity component. The formulation for the circumferential component Λ_w is analogous to equation (9).

B. Turbulence measurements downstream of the rotor

For the measurements of the rotor wake properties, we understand the velocity downstream of the rotor as a superposition of two independent processes: First the average velocity profile of the wake that is rotating phase locked with the rotor, and second the turbulence inside the wake that is fluctuating with an independent phase with respect to the rotor. To separate these two components, the time series of the velocity fluctuations are adaptively resampled and a cyclostationary analysis is performed [29]. In the next step the turbulence properties of the wakes are separated from the turbulence properties in the background flow with the method presented by Caldas and Meyer [30].

To characterize the rotor wakes, hot wire measurements were performed in the interstage section between rotor and stator at different operating conditions. The two probes are again mounted in the same axial plane with an angle of 17.1° which corresponds to the stator vane spacing. A photograph of the two probes behind the rotor is depicted in Fig. 4. This photograph was taken before the duct was closed for the test. The axial distance of the HW probes to the rotor trailing edge is 105 mm, see Fig. 9.

In the case with inflow distortion however, the wake properties measured at a single circumferential position cannot be extrapolated in the circumferential direction. The reason for that is, that the wakes are modulated by the inflow distortion. Hence, multiple measurements with the inflow distortion device in a rotating duct at 20 positions were carried out, resulting in a resolution of 18°.

IV. Acoustic measurements upstream of the fan

Measurements were performed with arrays of wall flushed microphones. A linear array of 30 microphones was used in combination with an ring array of 59 microphones (Fig. 5). For the broadband noise timelines of 120 s were recorded with a sampling frequency of 65 536 Hz. The time series of sound pressures are adaptively resampled and separated into rotor-coherent and rotor-incoherent components. In this work only the rotor-incoherent components are considered.

The measured sound pressure p at an arbitrary position $\boldsymbol{x}$ at each frequency is understood as a superposition of acoustic modes:

$$p(\boldsymbol{x}) = \sum_{m=-\infty}^{\infty} \sum_{n=0}^{\infty} \left(A^{+}_{mn} e^{jk^{+}_{mn}x} + A^{-}_{mn} e^{jk^{-}_{mn}x} \right) f_{mn}(r) e^{jm\vartheta}\,, \tag{10}$$

with $A^{\pm}_{mn}$ the amplitude of the acoustic mode of azimuthal order m and radial order n, $k^{\pm}_{mn}$ the axial wave number of acoustic mode, and $f_{mn}(r)$ the radial mode shape function. The superscript '+' indicates a downstream propagation of the mode and the superscript '-' upstream propagation.

Figure 4 Photograph of two hot wire probes, mounted downstream of the rotor

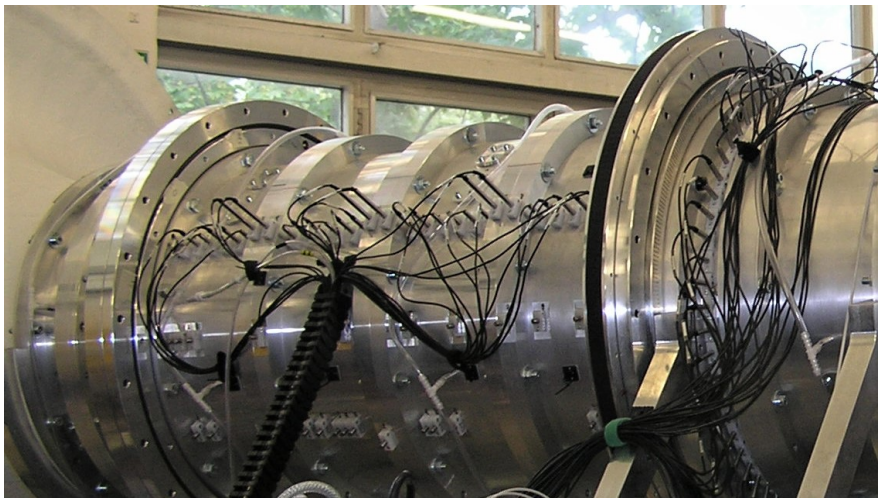

Figure 5 Photography of inlet microphone array

For the broadband sound field, the modes are assumed to be fully uncorrelated and and the expected values of the squared mode amplitudes are calculated with the combined axial and azimuthal sensor array (CAAS) method method. A compact description of the method is given by Tapken et al. [31]: „[The CAAS method] evaluates the cross spectral densities that are calculated for the sensors of the ring individually with each sensor of the axial line [...] and stores them into the vectors $\boldsymbol{S}_{p_o p_l(x_j)}$. The radial mode analysis is executed in two steps: First an azimuthal mode decomposition is performed, in the second step the expected values of the squared mode amplitudes $\left\langle \left|A_{mn}^{\pm}\right|^2 \right\rangle$ of the downstream and upstream propagating radial modes are determined by a least-square fit individually for each order m.“ Further details on the method are found in reference [25]. The high frequency limit of this method is determined by the length of the microphone array. Modes with the same azimuthal mode order are distinguished by the axial wavenumber. At high frequencies the axial wave numbers asymptotically tend towards the axial wave number of the plane wave. The more cut on the mode is, the closer its axial wave number is to this number. Hence, small radial mode orders can not be distinguished effectively by the method at higher frequencies. The modes with azimuthal order $m = 0$ are the first modes where this problem occurs. To resolve this, a longer axial array would be required. With the line array in the inlet the mode decomposition is robust for the modes with order $m = 0$ up to 6 kHz, which is about 4.5 times higher than the BPF

at maximum rotor speed. Above that frequency, the modes with small mode orders are systematically overestimated.

The sound power of the acoustic modes is then calculated based on the calculation of the intensity according to Morfey [32]:

$$P_{mn}^{\pm} = \frac{\pi R^2}{\rho c} \frac{\alpha_{mn}(1 - M_x^2)^2}{(1 \mp \alpha_{mn} M_x)^2} \left| A_{mn}^{\pm} \right|^2 , \tag{11}$$

where R is the duct radius, ρ the densit, c the speed of sound and, M_x the axial Mach number. The propagation factor α_{mn} is:

$$\alpha_{mn} = \sqrt{1 - (1 - M_x^2) \frac{\sigma_{mn}^2}{(kR)^2}} . \tag{12}$$

The definitions of eigenvalue σ_{mn} and the corresponding mode shape function f_{mn} are found in the literature, see e.g. Tapken [33].

V. Measurement results of different inflow distortions

In this section, the results of the hot wire measurements are presented. Firstly, the turbulence properties in the inlet are discussed. These are the defining parameters for the TRI noise source. Secondly, the turbulent rotor wakes are analysed at three operating conditions: the working line, high pressure ratio and high mass flow. Lastly, the effect of the inflow distortion on the turbulent rotor wakes is discussed. The results are discussed regarding the broadband noise excitation in section VII.

A. Turbulence measurements of inflow distortion profile

In the following figures, the inflow distortion profile in the inlet section is compared to the clean configuration and to a theoretically modelled profile. The distorted profile is evaluated at the circumferential position with the largest boundary layer thickness, i.e. in the center of the distortion. Because modelling the boundary layer of a full scale fuselage with a boundary layer ingestion engine inlet would go beyond the scope of this study and no sufficient measurements of realistic BLI turbulence are known to the authors, a one dimensional analytical model is used to give a reference profile. Staggat [34] describes the model that uses the boundary layer thickness δ_{99} and the shape factor H_{12} as arbitrary input parameters to calculate not only the mean flow profile, but also the turbulence intensities and length scales. The shape factor of a fully developed flow profile with no pressure Gradient is expected to be 1.3. Values with $H_{12} < 1.3$ experience a negative pressure gradient, that means the fluid is accelerated and the profile is stabilized. For larger values $H_{12} > 1.3$ the pressure gradient is positive and the fluid is decelerated and the boundary layer is destabilized and may even separate. When the shape factor reaches the value 4.0 the boundary layer is separated [34].

The turbulence properties from the model should not be regarded as reference values of a realistic fuselage boundary layer but as a first approximation. Advanced analytical fan noise prediction models might be able to take the BLI profile into account. Then the model may be used as a tool to enable parameter studies for different fan noise sources, similar to Staggats work [34].

In Fig. 6 the average axial velocities of the distorted and clean configuration are shown. The logarithmic profile is modelled to match the properties of the distorted flow profile.

For a quantitative Comparison of the Profiles, the boundary layer thickness δ_{99}, the displacement thickness δ_1, the momentum thickness δ_2 and the shape factor H_{12} of the inflow distortion profiles are summarized in Tab. 2 The boundary layer δ_{99} of the clean case is calculated to be almost 80 mm, which is 35 % of the duct radius. Because of the slightly parabolic shape of the free flow in the clean case, the δ_{99} does not well represent the boundary layer thickness. The δ_{95} Value for this profile is 14.2 mm, which is still 6 % of the duct radius.

In Fig. 7 the axial and radial components of the turbulence intensities are shown. The clean configuration develops a typical turbulent wall boundary layer with turbulence Intensities up to 10 %. Outside the boundary layer, the turbulence intensities are below 1 %. A continuous increase of the turbulence intensity towards the duct wall is reached with the distortion. This profile shows similarities with a thick boundary layer. Although the turbulence intensities of up to 30 % in the axial direction are much higher than for the boundary layer of the clean configuration. The modelled profile

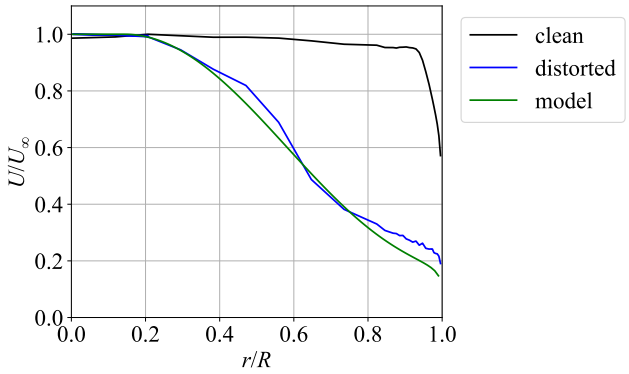

Figure 6 Mean flow velocity profiles, measured with hot wire probes in measurement plane E3.

Table 2 Boundary layer properties of the different profiles

Profile	clean	distorted	log
δ_{99} in mm	79.4	179.5	180.0
δ_{95} in mm	14.2	162.1	162.2
δ_1 in mm	4.6	71.9	76.4
δ_2 in mm	3.7	30.6	30.6
H_{12}	1.23	2.35	2.50

reaches a maximum for the axial component of turbulence intensity of more than 20 % at $r/R \approx 0.7$, and is reduced to zero towards the duct wall. Here we have a discrepancy between the modelled boundary layer and the distorted flow profile. All profiles show anisotropic turbulence, i.e. the axial turbulence intensity is higher than the radial turbulence intensity.

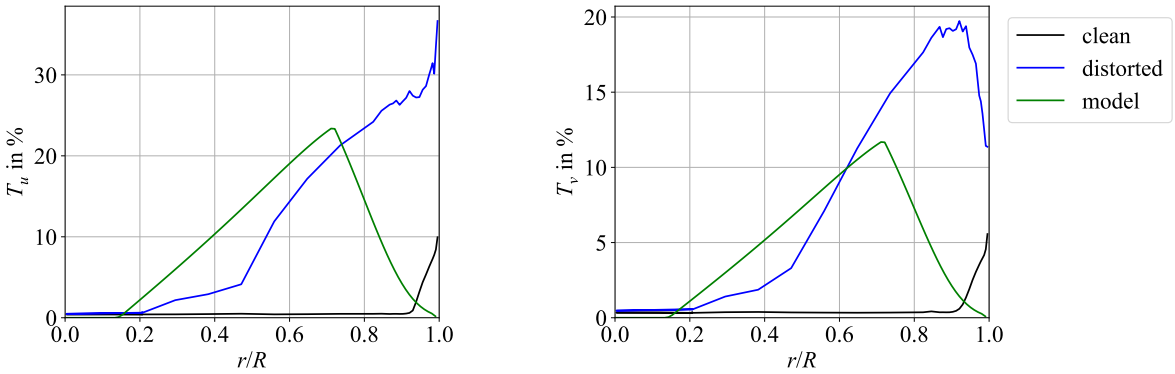

Figure 7 Turbulence intensities, measured with HW1 in measurement plane E3. Axial component (left) and radial components (right)

In the theory of TRI noise, the turbulence kinetic energy (TKE) in the inflow is a commonly used quantity. For example, in the model formulated by Moreau [35] the excited sound power level scales directly with the TKE. In Fig. 8 on the left the turbulence kinetic energy is shown. Here the axial and radial components of the turbulence are used and an axisymmetric turbulence spectrum is assumed, i.e. $\tilde{w} = \tilde{v}$. The clean configuration features higher values of TKE only in the boundary layer. The TKE of the distortion reache high values in a relatively large area. Nonetheless, The predicted TKE of the boundary layer model is even higher.

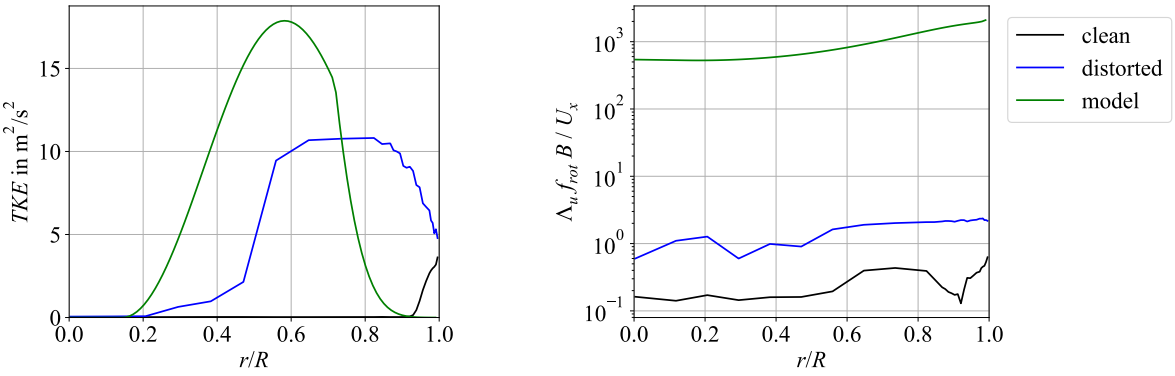

Figure 8 TKE (left) and Λ_x (right), measured with HW1 in measurement plane E3

The turbulent length scale is also considered very important for the shape of the excited acoustic spectrum and for the excited sound power of the TRI noise. The length scale determines whether haystacking is to be expected. For this effect the ratio between the time an eddy needs to travel through a fixed plane must be larger than the time of a blade passage [13, 17]. Or, more precisely

$$\Lambda f_{\mathrm{rot}} B / U_x \gg 1 \tag{13}$$

must hold. Therefore the axial length scale is normalized to resemble this criterion. As is visible in Fig. 8 on the right, the experimentally determined length scales are two orders of magnitude smaller than the length scale in the boundary layer model. Nevertheless, the turbulence length scales in the distorted flow are bigger than in the clean flow and the criterion from equation (13) reaches Values larger 1 near the duct wall and small haystacking might be expected for this inflow distortion. Even for the clean case the normalized length scale is close to 1 in the boundary layer.

B. Average and turbulence flow properties of the rotor wakes

Hot wire measurements were executed at three axial positions, 25 mm, 65 mm and 105 mm behind the rotor. The acoustic measurements were analyzed with the medium distance of 92 mm between the rotor trailing edge and the stator leading edge. The results presented in this section were measured with the long distance, as this case is considered most representative for the acoustic RSI source at the medium distance configuration. For clarity, the axial spacing of the hot wire measurements and the acoustic measurements is depicted in Fig. 9.

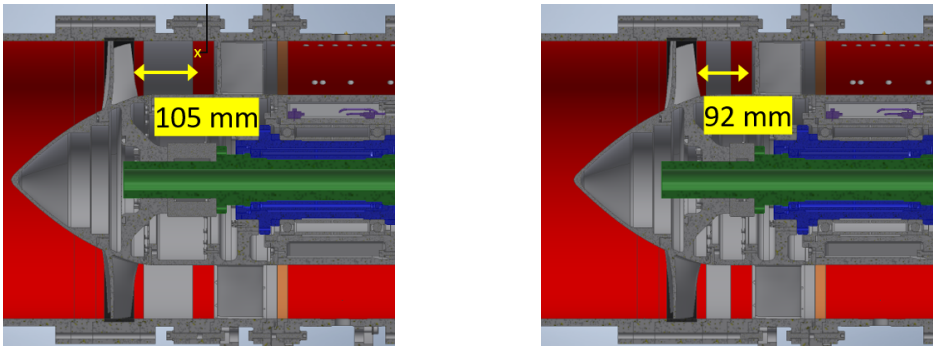

Figure 9 Rotor stator spacing for hot wire measurements (left) and acoustic measurements (right).

All measurements were performed at 4500 RPM rotation speed. The different operating conditions are described by means of the flow coefficient

As already mentioned above, the velocity of rotor wakes can be understood as a superposition of the average velocities that are characterized by the velocity deficit of the wakes, and the turbulence of the wakes. To visualize these two

processes, the resampled time series of one rotor revolution of the velocity behind the rotor is plotted in Fig. 10 in blue together with the ensemble average of all rotor revolutions in black. Shown here is only the axial component of the velocity vector, as measured with HW2. Due to the swirl behind the rotor, the HW2 probe is considered more accurate, because it can be used to separate the axial and the circumferential velocity component. The operating conditions are 4500 RPM and $\Phi = 0.33$. The turbulent fluctuations stand out in comparison to the mean velocity deficit of the wakes.

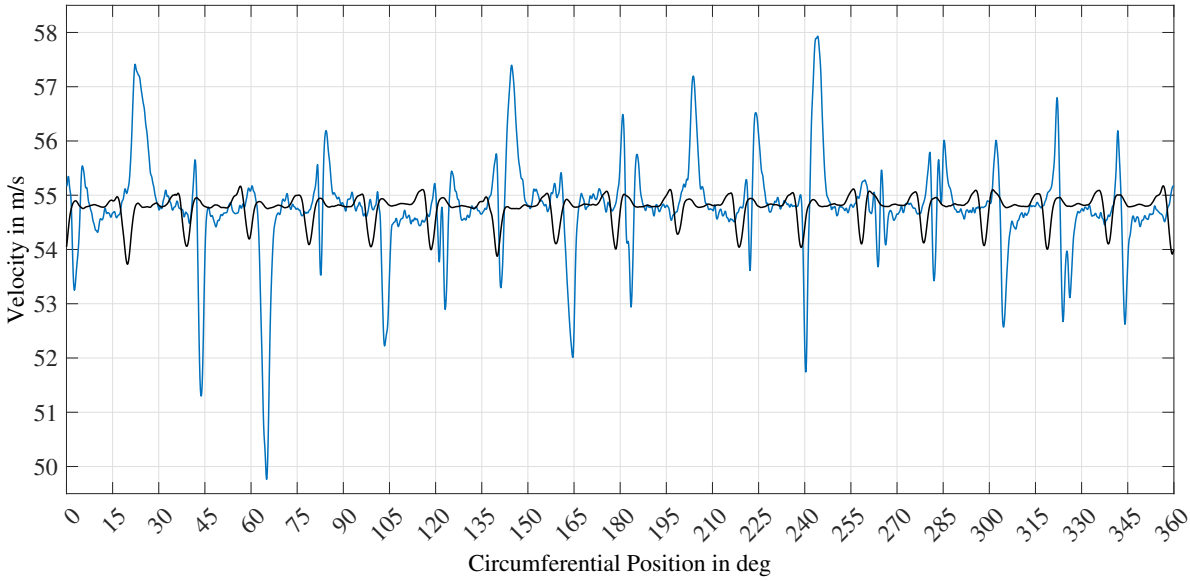

Figure 10 Rotor wakes at 50% relative radial height for different axial distances, left is the mean and right is the rms axial velocity, measured with HW2.

Noteworthy is the overshooting that is not only present in the turbulent fluctuations, but also in the ensemble averaged velocities. Hot wire measurements of rotor wakes in the literature do not show this behaviour. Jenkins [36] analyzed hot wire measurements at three axial positions behind the ACAT-1 fan which is representative in size and Mach number for an aircraft engine. The wake width of the rotor that Jenkins studied was broadened downstream of the rotor to an extend that the wakes overlapped and the measured flow profile converged to a single sine profile. In Contrast, the wakes of the CRAFT remain limited with respect to the width and display an overshooting in the average velocity. At the moment it is not clear whether this difference in the broadening of the wakes can be explained with the different Reynolds numbers and chord lengths or whether there is a different explanation.

In Fig. 11 the velocities from HW2 for the axial and circumferential component are combined. Here only the velocity component in the direction of the mean flow vector is shown. On the left of Fig. 11 the average velocity deficit is shown for three operating points: High loading ($\Phi = 0.28$), reference working line ($\Phi = 0.33$) and high volume flow ($\Phi = 0.40$). The velocity profile is subtracted from the free flow velocity U_∞, i.e. the average velocity outside the wake region.

The velocity deficit is smallest for the high loading case and largest for the high volume flow case. The same trend holds for the overshooting. On the contrary, the wake width and velocity variances are smallest for the high volume flow operating condition and largest for the high loading operating condition. The wake width is estimated based on the rms value of the velocity as described by Caldas and Meyer [30], see also Fig. 11 right. The shape of the rms velocities on the pressure side, that is for $\theta > 0$, are similar for $\Phi = 0.33$ and $\Phi = 0.4$. However, on the suction side the boundary layer appears further reduced with the high volume flow because of the negative incidence. An explanation for this non-symmetric wake shape is the laminar separation bubble at the transition point on the suction side. The transition is typical for low Reynolds numbers between $2 \cdot 10^5$ and $2 \cdot 10^6$ [37]. With the blade chord of 62 mm, the Reynolds number is between $4.5 \cdot 10^5$ at the high loading operating point and $5.2 \cdot 10^5$ at the high volume flow operating point.

In Fig. 12 the free flow velocity, the swirl angle and the turbulence kinetic energy in and outside the wake are shown over the scaled radius $\tilde{r} = \frac{r - R_h}{R - R_h}$, where R_h is the hub radius.

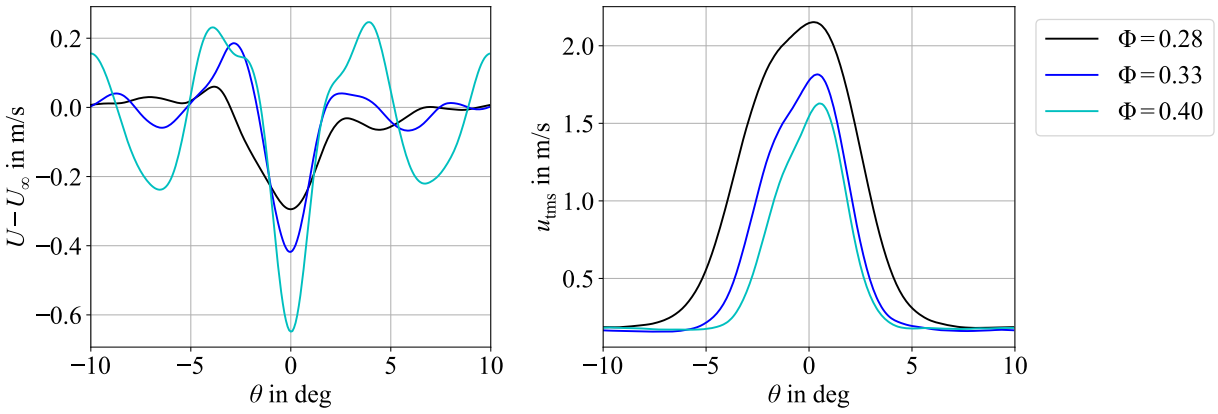

Figure 11 Rotor wakes at 4500 RPM at 50 % relative radial height for three different flow coefficients. Left is the mean and right is the rms velocity in stream wise direction, measured with HW2.

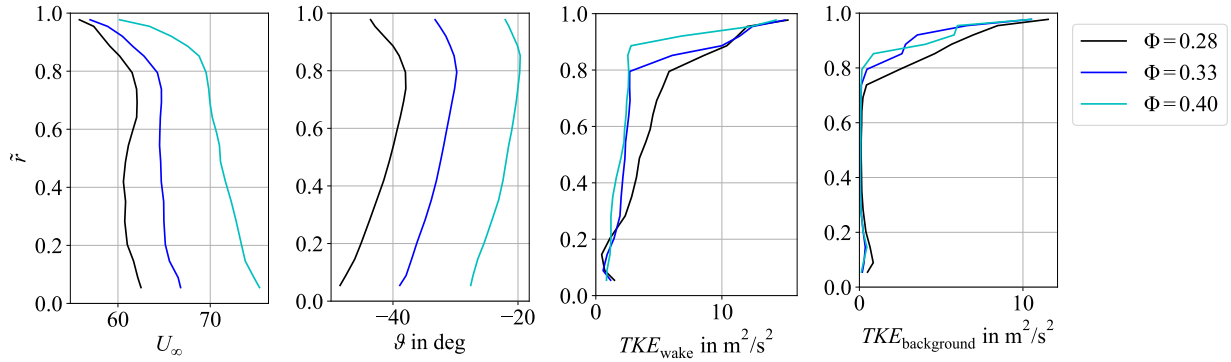

Figure 12 Rotor wake properties a) average flow velocity in stream wise direction, b) swirl angle, c) turbulence kinetic energy inside the wake, d) turbulence kinetic energy in background flow.

The free flow velocity U_∞ is the absolute value of the velocity vector outside the wake and reaches its maximum near the hub for all operating points. For the high loading case a local maximum is reached at about 70 % of the duct height. The swirl angle is negative. Following our convention of the right hand coordinate system with positive x axis pointing in flow direction, the rotor is rotating in negative θ-direction. The minima of the swirl are near the duct and hub walls. Near the hub the flow follows the rotor rotation and near the duct wall, the average flow is strongly affected by the tip vortex. The turbulence kinetic energies for the operating conditions $\Phi = 0.4$ and $\Phi = 0.33$ are similar up to $\tilde{r} = 0.7$. The region influenced by the tip vortex is larger for $\Phi = 0.33$. The TKE is highest for $\Phi = 0.28$. The TKE in the background flow is dominated by the tip vortex. The tip vortex is increased with the loading.

C. influence of inflow distortion on the turbulent rotor wakes

In Fig. 13 the average and rms velocity in stream wise direction are shown. The operating point is the working line reference ($\Phi = 0.33$) and the coloured lines correspond to different relative angles $\Delta\theta$ between the hot wire probe position and the center of the distortion. The velocity deficit ranges from -0.3 m/s to -0.9 m/s, which is more than the variation of different operating conditions. Due to the negative swirl, the strongest effects are measured at $9° \leq \Delta\theta \leq 63°$. In this region rather large rms velocities are measured on the suction side outside the wake, which indicates a flow separation because of the distorted inflow.

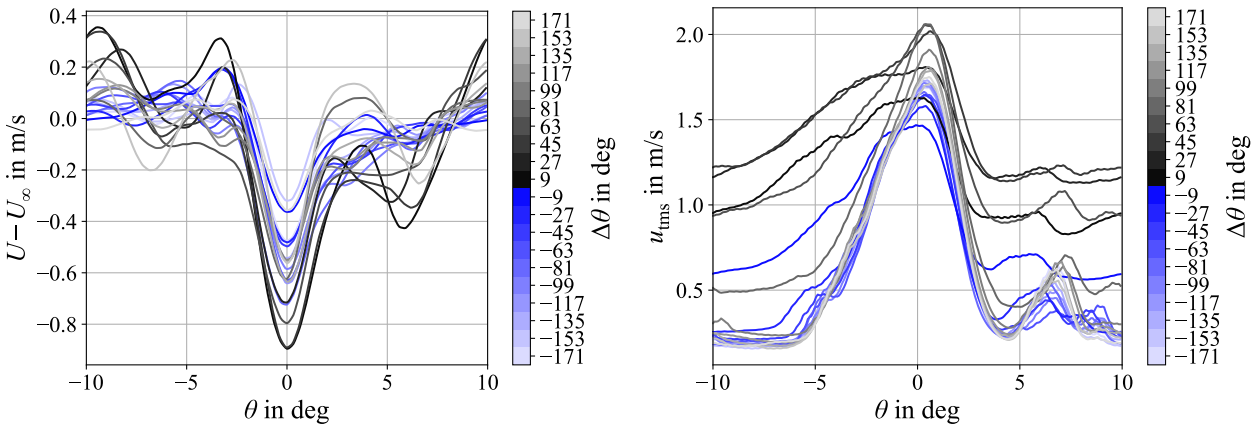

Figure 13 Distortion effect on rotor wakes at 50% relative radial height for different relative positions of hot wire probe and distortion, left is the mean and right is the rms velocity in stream wise direction, measured with HW2, $\Phi = 0.33$.

In Fig. 14 the free flow velocity, the swirl angle and the turbulence kinetic energy in and outside the wake are shown over the scaled radius for the different relative angular positions of the inflow distortion. Interestingly, the free flow velocity is minimal where the blade immerses into the distortion, and is maximal were the blade emerges from the distortion. A similar behaviour is observed for the swirl angle. The minimal value is reached for small relative angles ($-45° \leq \Delta\theta \leq 9°$), where the blade immerses into the distortion. This corresponds to the highest loading. The largest swirl angles (minimal loading) are measured right after the blade emerges from the distortion into the free flow ($63° \leq \Delta\theta \leq 117°$).

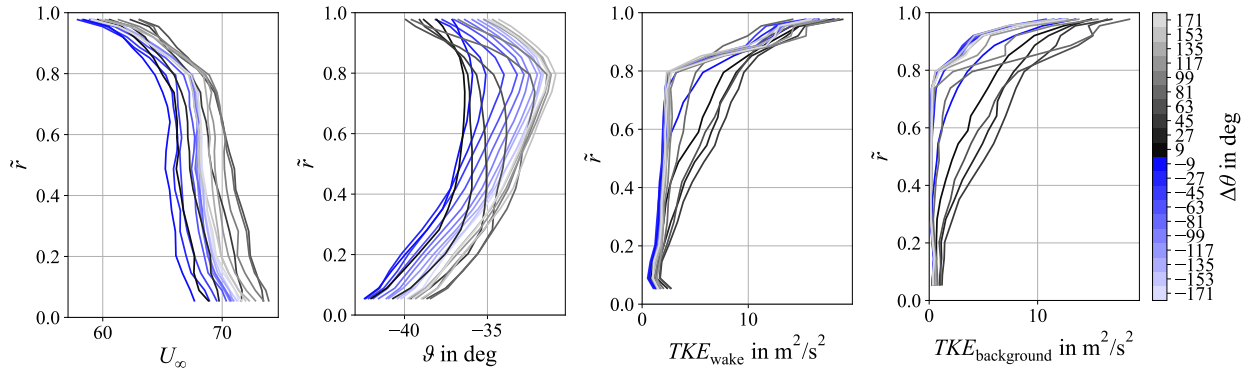

Figure 14 Distortion effect on rotor wake properties a) average flow velocity in stream wise direction, b) swirl angle, c) turbulence kinetic energy inside the wake, d) turbulence kinetic energy in background flow, $\Phi = 0.33$.

The TKE inside the wake is increased for relative angles $9° \leq \Delta\theta \leq 81°$ between 20 % and 80 % of duct height. In the hub region the TKE is barely affected and in the tip region the tip vortex dominates the turbulence. The separation in the distorted area, that is visible in the rms velocities in Fig. 13 is also visible in the TKE of the background flow. The separation seems stronger towards the tip of the blade, where the separation blends into the tip vortex.

VI. Sound power level measurements

In Fig. 15 the modal sound power levels of all upstream propagating modes measured in the inlet are displayed at 4500 RPM and for the flow coefficients $\Phi = 0.28$ on the left and $\Phi = 0.33$ on the right. Where more than one radial mode

order is cut on, the mode sound powers are summed. Above 4 BPF the used method systematically overestimates the mode amplitudes of the low mode orders, starting at the $m = 0$ modes.

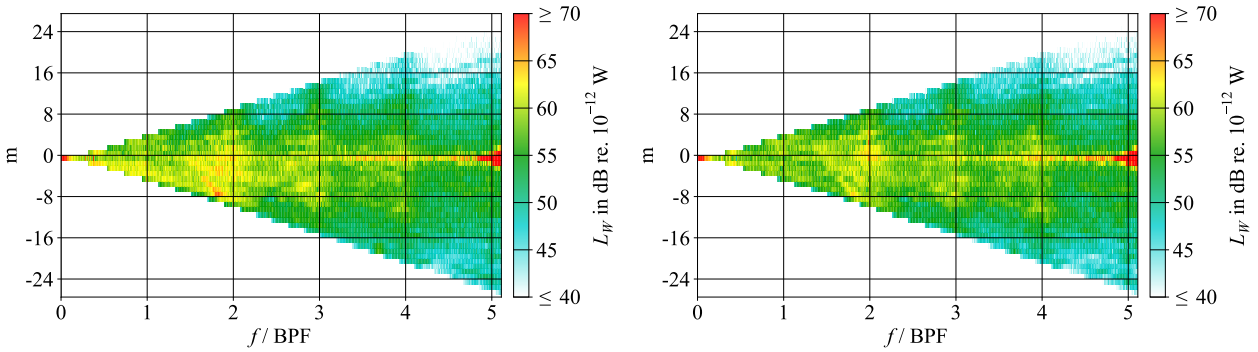

Figure 15 Sound power level of azimuthal modes summed over all upstream propagating radial mode orders, clean configuration. Left: high loading, $\Phi = 0.28$, right: working line, $\Phi = 0.33$.

The results of the high loading case show an asymmetry with higher power levels for modes with $m < 0$. This asymmetry is especially pronounced below 2 BPF. These modes are co-rotating with the rotor. Our interpretation is, that these modes originate from a sound source downstream of the rotor, likely RSI. Although all modes are excited by the RSI, the counter-rotating modes tend to be shielded by the rotor and in the measurement upstream of the rotor the co-rotating modes predominate the mode spectrum [38].

In Fig. 16 the modal sound power levels of all upstream propagating modes measured in the inlet are shown for the distorted case. The operating conditions are again at 4500 RPM with the flow coefficients $\Phi = 0.28$ on the left and $\Phi = 0.33$ on the right. Both figures show a distinct increase in sound sound power, relative to the clean case. The Increase is the most pronounced around the first BPF. However, the differences between the two operating conditions are hard to spot with the bare eye.

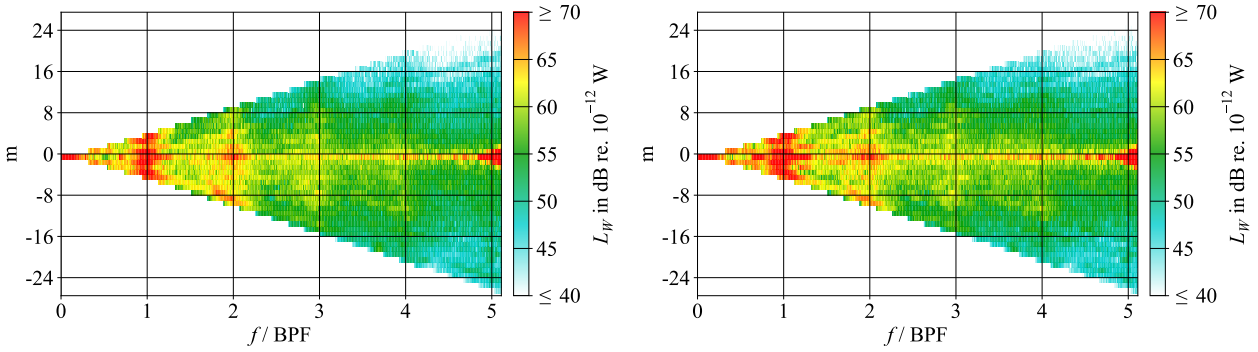

Figure 16 Sound power level summed over all upstream propagating radial mode orders, distorted configuration. Left: high loading, $\Phi = 0.28$, right: working line, $\Phi = 0.33$.

For a quantitative comparison the sound power levels of azimuthal modes PWL(m) are summarized over all propagating modes, in other words along the y axis of Figs. 15 and 16. The result can be observed in Fig.17. On the left the summed PWL of all upstream propagating modes are shown for the three operating points for the clean configuration, on the right for the distorted configuration. For the clean case the PWL similar for all Φ. The PWL for the high loading case is elevated between BPF and 2 BPF. The clean PWL spectra have a wavy shape. This shape can be attributed to the boundary layer that interacts with the rotor and is comparatively thick due to the long inlet [39].

In the distorted cases (see Fig 17 right) the spectra have a wide maximum around BPF. Furthermore the trends are contrary to the clean configuration in the sense, that the high volume flow operating point leads to the highest sound

power excitation. This leads to the conclusion, that TRI is a strong noise source in this configuration, because the TRI scales directly with the inflow velocity.

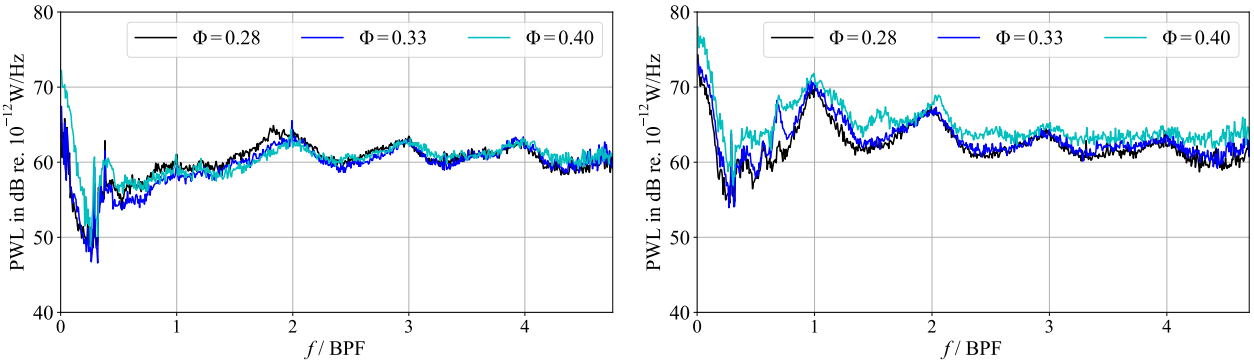

Figure 17 Sound power level summed over all upstream propagating radial and azimuthal mode orders, clean (left) and distorted (right) configuration.

In Fig. 18 the sound powers of all modes that are co-rotating with the rotor are summarized for different operating conditions for the clean and distorted configuration. For the clean configuration, the trend of the RSI source is visible: Up to 3 BPF the sound power rises with the loading. Only small differences between the high loading and working line operating points are visible for the distorted configuration. The high mass flow operating point shows an increase of broadband noise, mostly between the BPF harmonics.

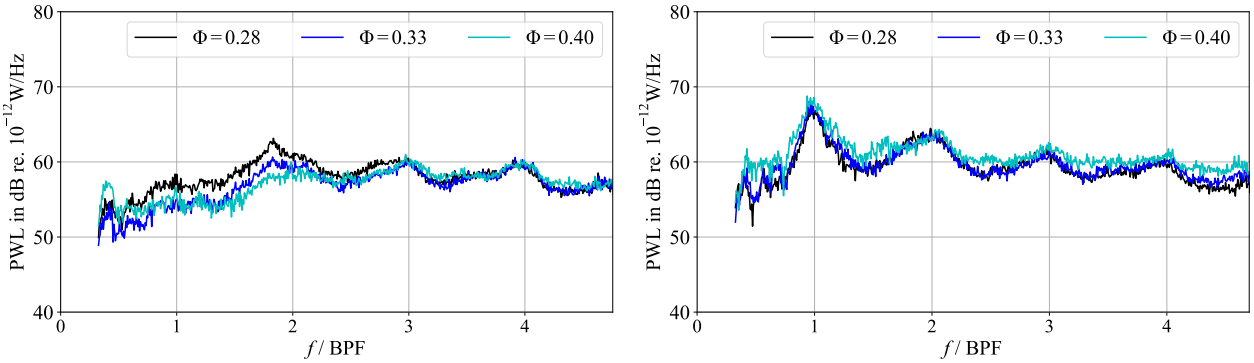

Figure 18 Sound power level summed over all upstream propagating radial and azimuthal mode orders co-rotating with the rotor, i.e. $m < 0$, clean (left) and distorted (right) configuration.

The summed sound powers for all modes that are counter-rotating with the rotor are plotted in Fig. 19, again at different operating conditions for the clean and distorted configuration. For the counter-rotating modes, in the clean case the deviations between the operating points are small. In the distorted case however, a clear trend is measured. The sound power level is increased with the flow coefficient. This behavior fits to the source of TRI. Especially between the BPFs the sound power is increased. As the turbulence length scales are small, we expect a flat sound power spectrum to be excited from the TRI. The maximum at BPF is much less affected by the flow coefficient. At this frequency component an additional source mechanism can be expected that is likely related to the flow detachment on the rotor blades, where the rotor enters the inflow distortion, as observed in section V.C.

The summed sound powers for all modes with mode order $m = 0$ at different operating conditions for the clean and distorted configuration are shown in Fig. 20. The strong contribution below BPF coincides with the cut on frequency of the first nonzero radial mode order.

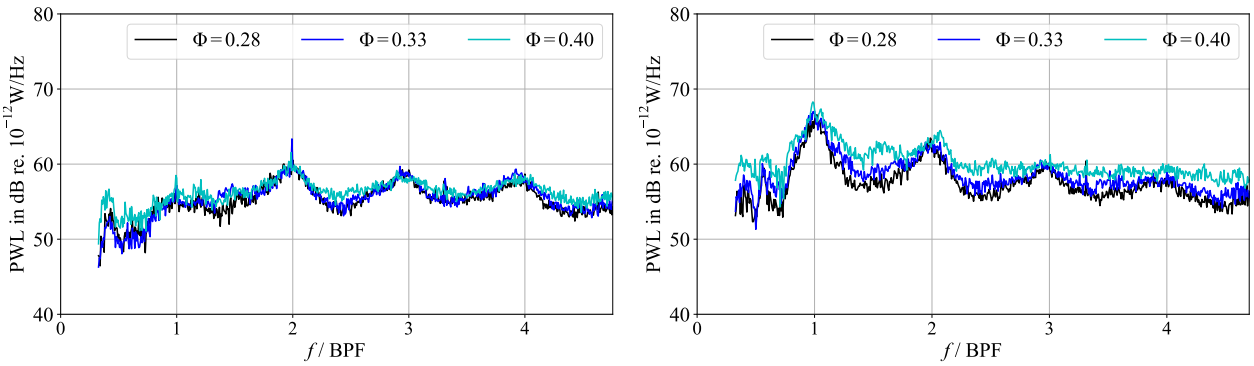

Figure 19 Sound power level summed over all upstream propagating radial and azimuthal mode orders counter-rotating with the rotor, i.e. $m > 0$, clean (left) and distorted (right) configuration.

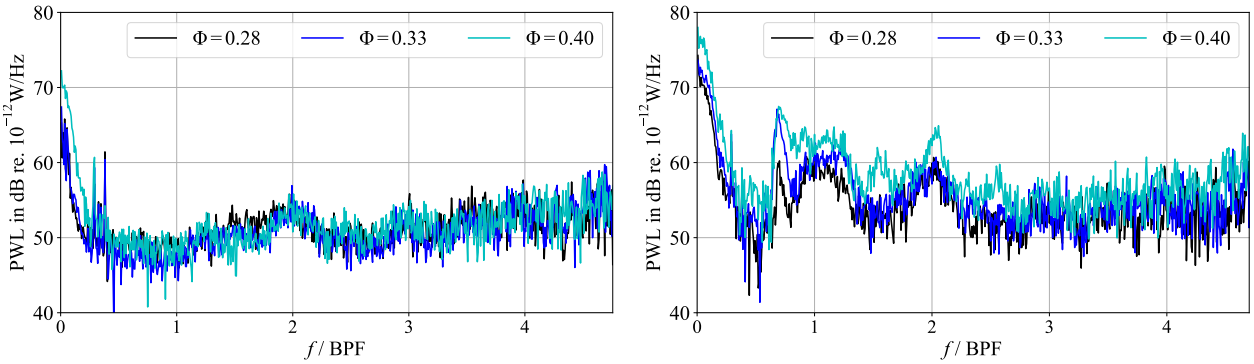

Figure 20 Sound power level summed over all upstream propagating radial mode orders with azimuthal order $m = 0$, clean (left) and distorted (right) configuration.

VII. Summary, discussion and outlook

In the context of emerging engine designs with relevant inflow distortions we expect a drastic increase of the noise emission. We used an experimental approach, to learn about the effects of inflow distortion on fan noise at subsonic conditions. We measured the acoustic modes with flush mounted microphones and captured the fluctuating flow field in the inlet and the effect on the rotor wakes with hot wire anemometers. The present paper supplies a phenomenological basis for further research on the effects of inflow distortion on different fan noise sources. In this section the results are interpreted and a hypothesis on the most relevant noise source mechanisms with and without inflow distortions is formulated.

Low turbulence intensity and small length scales in the free flow and a distinct boundary layer due to the long inlet characterize the Inflow conditions in the clean case. The operating point substantially influences the measured rotor wakes in the clean configuration. The wake width and TKE increase with the blade loading. The RSI is closely related tor the rotor wakes turbulence and increases with blade loading as well. On the contrary the TRI noise increases with the inflow turbulence and inflow velocity. With analytical prediction methods, Klähn et al. [40] showed that the RSI noise is the strongest fan noise source at high loading while at high mass flows the TRI noise is the strongest fan noise source for subsonic axial fans. This trend was not as clear in the experimental data as in the analytical predictions. The co-rotating modes upstream the rotor contain most of the sound power from the RSI, because the counter-rotating modes are shielded by the rotor. In the present acoustic measurements, if only the co-rotating modes are considered, the trend that RSI noise is reduced with increased flow rate can be identified in the clean configurations, see Fig. 18.

In the case with the inflow distortion, the wakes shape and turbulence properties depend on the relative position of the wake with respect to the inflow distortion. In the rotating reference frame, the wake properties vary periodically with each rotation. As the inflow distortion impacts the turbulence in the wakes strongly, one would expect an impact on broadband RSI noise as well. But the acoustic results do not reflect this. Our hypothesis why no clear effect on

broadband RSI noise is measured is, that other noise sources mask the RSI noise. Which noise source mechanism is dominant in the present study is not completely clear to the authors and further research on this question is required, but some candidates can be identified and discussed. These sources are the TRI, boundary layer interaction noise, separation noise or stall noise [41] and tip vortex noise.

The TRI is the noise source that is mostly considered in the context of inflow distortion noise. As we have high TKE in the inflow, it is plausible, that this is a relevant noise source. Also the fact that the sound power level is increased with the flow coefficient supports this. Because of the small turbulence length scales measured in the inflow distortion, this noise source should generate a flat spectrum. And in fact the spectrum is flattened in the distorted case above 2 BPF. Furthermore, no spectral broadening around 3 BPF and 4 BPF are visible for the counter-rotating modes at the highest flow coefficient. However, the maxima around BPF and 2 BPF, that vary only slightly with the flow coefficient, can not be explained with TRI noise.

The boundary layer at the rotor plane is considerable because of the long inlet. Ganz et al. [39] attribute the wavy shape of the spectrum in the clean configuration to the boundary layer interaction noise. The authors explain the shape with the turbulence length scale, which is small in the boundary layer. This seems to contradict the statement in the previous paragraph about the TRI noise that the small length scales in the inflow lead to a flat spectrum. Equation (13) might resolve this contradiction. If the axial velocity in the boundary layer is sufficiently small, blade to blade correlations can occur, see also Fig. 8. Therefore, in the clean configurations this noise source might be dominant above 2 BPF. In the distorted case the boundary layer in the free flow is not expected to increase substantially and the interaction of the turbulent distortion Profile should be regarded as TRI. Therefore the boundary layer interaction noise is no explanation of the maxima at BPF and 2 BPF as well.

The turbulence measurements downstream of the rotor show large TKE values in the background flow in the area of the distorted inflow. This strong turbulence could be convected inflow turbulence. It could however, also be the result of flow detachment due to the large incidence angles. The way the rms velocities in the wake fade into the background turbulence support the latter hypothesis. This detachment would cause a periodic on and off excitation of stall noise. Stall noise has a low frequency spectrum, but the periodic on and off switching of this source would create a maximum around the BPF.

The noise which is related to the tip vortex depends not only on the tip clearance, but also on the operating conditions [42]. Similar to the RSI noise, we expect the tip vortex noise to be increased with higher loading (or smaller inflow velocity) because the tip vortex is increased with the loading. As is confirmed by our hot wire measurements behind the rotor in the clean case. In the distorted case, the tip vortex depends on the relative position to the inflow distortion and contains a large part of the TKE. Hence, an increase of tip vortex noise from the clean case to the distorted case is plausible. However, the tip vortex noise is still expected to be further increased at small flow rates, but the sound power spectra show the smallest values at small flow rates. Therefore the tip vortex noise is presumably not the strongest noise source in the distorted case. Nonetheless, the relationship between tip vortex noise, inflow distortion and operating conditions may be more complex than outlined in this paragraph and should be investigated further.

The conclusion from the presented experimental study can be summarized with following hypothesis. In the clean configuration the spectrum is mainly composed of RSI noise at low frequencies and boundary layer noise at high frequencies, while for the distorted configuration the spectrum is mainly composed of stall noise at low frequencies and TRI noise at high frequencies.

To support or falsify this hypothesis further experiments and aeroacoustic noise predictions are appropriate. Further experiments with the same rotor but without the stator would help to separate the RSI noise from the rotor noise sources. Measurements with a short intake should reduce the boundary layer noise and help to estimate the relation between RSI and boundary layer noise in the clean case. Additionally, aeroacoustic predictions of the discussed noise sources could help to confirm or oppose the hypothesis. In this regard the predictions must take into account the non-stationary on and off excitation of these noise sources. The boundary layer model that was used for comparison in section V.A could be used for parameter studies of these noise sources. An extension of the known RSI prediction methods to take into account the modulation of the rotor wakes would be required as well.

Acknowledgments

This work would not have been possible without the accommodating support of multiple colleagues at DLR Berlin. The authors thank Wolfram Köhler for the joint planning, preparation and execution of the experiments. Furthermore the authors thank Angelo Rudolphi, Sebastian Kruck and Sven Nieländer for their technical support that made the operation of the test rig possible in the first place.

References

[1] Seitz, A., Habermann, A. L., Peter, F., Troeltsch, F., Castillo Pardo, A., Della Corte, B., van Sluis, M., Goraj, Z., Kowalski, M., Zhao, X., Grönstedt, T., Bijewitz, J., and Wortmann, G., "Proof of Concept Study for Fuselage Boundary Layer Ingesting Propulsion," *Aerospace*, Vol. 8, No. 1, 2021, p. 16. doi:10.3390/aerospace8010016.

[2] Gunn, E. J., and Hall, C. A., "Aerodynamics of Boundary Layer Ingesting Fans," *Turbo Expo: Power for Land, Sea, and Air*, Vol. Volume 1A: Aircraft Engine; Fans and Blowers, 2014. doi:10.1115/GT2014-26142.

[3] European Commission, Directorate-General for Mobility and Transport, Directorate-General for Research and Innovation, *Flightpath 2050 – Europe's vision for aviation – Maintaining global leadership and serving society's needs*, Publications Office, 2011. doi:10.2777/50266.

[4] Kobayashi, H., and Groeneweg, J. F., "Effects of inflow distortion profiles on fan tone noise," *AIAA Journal*, Vol. 18, No. 8, 1980, pp. 899–906. doi:10.2514/3.50832.

[5] Daroukh, M., Polacsek, C., and Carini, M., "Acoustic Assessment of BLI Effects on Airbus Nautilius Engine Integration Concept - Part I: Noise Generation," *28th AIAA/CEAS Aeroacoustics 2022 Conference*, 2022. doi:10.2514/6.2022-2943.

[6] Klähn, L., Caldas, L., Meyer, R., Moreau, A., and Tapken, U., "Experimental Investigation of Inflow-Distortion-Induced Tonal Noise in a Sub-Sonic Fan Test Rig," *Proceedings of the 29th International Congress on Sound and Vibration*, edited by International Institute of Acoustics and Vibration, 2023. URL `https://elib.dlr.de/194810/`.

[7] Guérin, S., Kissner, C. A., Kajasa, B., Jaron, R., Behn, M., Pardowitz, B., Tapken, U., Hakansson, S., Meyer, R., and Enghardt, L., "Noise prediction of the ACAT1 fan with a RANS-informed analytical method: success and challenge," *25th AIAA/CEAS Aeroacoustics Conference*, American Institute of Aeronautics and Astronautics, Reston, Virginia, 2019. doi:10.2514/6.2019-2500.

[8] Guérin, S., Kissner, C., Seeler, P., Blázquez, R., Carrasco Laraña, P., de Laborderie, H., Lewis, D., Chaitanya, P., Polacsek, C., and Thisse, J., "ACAT1 Benchmark of RANS-Informed Analytical Methods for Fan Broadband Noise Prediction: Part II—Influence of the Acoustic Models," *Acoustics*, Vol. 2, No. 3, 2020, pp. 617–649. doi:10.3390/acoustics2030033.

[9] Lewis, D., de Laborderie, J., Sanjosé, M., Moreau, S., Jacob, M. C., and Masson, V., "Parametric study on state-of-the-art analytical models for fan broadband interaction noise predictions," *Journal of Sound and Vibration*, Vol. 514, 2021, p. 116423. doi:10.1016/j.jsv.2021.116423.

[10] Klähn, L., Caldas, L., and Tapken, U., "Measurements of fan inflow distortion noise generation in a low speed fan-part II: acoustic analyses," *28th AIAA/CEAS Aeroacoustics 2022 Conference*, Southampton, UK, 2022, p. 2945.

[11] Hanson, D. B., "Spectrum of rotor noise caused by atmospheric turbulence," *Journal of the Acoustical Society of America*, Vol. 56, No. 1, 1974, pp. 110–126. doi:10.1121/1.1903241.

[12] Majumdar, S. J., and Peake, N., "Noise generation by the interaction between ingested turbulence and a rotating fan," *Journal of Fluid Mechanics*, Vol. 359, 1998, p. 181–216. doi:10.1017/S0022112097008318.

[13] Homicz, G. F., and George, A. R., "Broadband and discrete frequency radiation from subsonic rotors," *Journal of Sound and Vibration*, Vol. 36, No. 2, 1974, pp. 151–177. doi:10.1016/S0022-460X(74)80292-0.

[14] Kerschen, E. J., and Gliebe, P. R., "Noise Caused by the Interaction of a Rotor with Anisotropic Turbulence," *AIAA Journal*, Vol. 19, No. 6, 1981, pp. 717–723. doi:10.2514/3.50995.

[15] Moreau, A., and Oertwig, S., "Measurements compared to analytical prediction of the sound emitted by a high-speed fan stage," *19th AIAA/CEAS Aeroacoustics Conference*, American Institute of Aeronautics and Astronautics, Reston, Virginia, 2013. doi:10.2514/6.2013-2047.

[16] Staggat, M., Moreau, A., and Guérin, S., "Improved analytical prediction of Boundary-Layer induced rotor noise using circumferential modes," *FAN 2018, International Conference on Fan Noise, Aerodynamics, Applications and Systems*, Darmstadt, Germany, 2018.

[17] Hickling, C. J., "Inhomogeneous, Anisotropic Turbulence Ingestion Noise in Two Open Rotor Configurations," PhD Thesis, Virginia Polytechnic Institute and State University, Blacksburg, Virginia, 2020. URL https://vtechworks.lib.vt.edu/handle/10919/100637.

[18] Caldas, L., Klähn, L., Meyer, R., and Tapken, U., "Measurements of fan inflow distortion noise generation in a low speed fan – part I: aerodynamic analyses," *28th AIAA/CEAS Aeroacoustics Conference*, Southampton, UK, 2022. doi:10.2514/6.2022-2944.

[19] Tapken, U., Caldas, L., Meyer, R., Behn, M., Klähn, L., Jaron, R., and Rudolphi, A., "Fan test rig for detailed investigation of noise generation mechanisms due to inflow disturbances," *AIAA AVIATION 2021 FORUM*, 2021. doi:10.2514/6.2021-2314.

[20] Kajasa, B., Lengyel, T., and Meyer, R., "Numerical and Experimental Design of a radial displaceable Inlet Distortion Device," *25th ISABE*, Ottawa, Canada, 2022.

[21] Lengyel-Kampmann, T., Karboujian, J., Koc, K., Schnell, R., and Winkelmann, P., "Experimental investigation on a lightweight, efficient, counter-rotating fan with and without boundary layer ingestion," *CEAS Aeronautical Journal*, 2024. doi:10.1007/s13272-024-00717-x.

[22] Meyer, R., Tapken, U., Klähn, L., Behn, M., and Lengyel-Kampmann, T., "Unsteady flow, turbulence and acoustic measurements on the counterrotating DLR turbo fan stage CRISPmulti, with and without inlet distortions," *Proceedings of ASME Turbo Expo 2024, Turbomachinery Technical Conference and Exposition, GT2024*, London, United Kingdom, 2024.

[23] Meyer, R., Knobloch, K., and Hakansson, S., "Hot-wire measurement in a Direct Driven high speed Turbo Fan (DDTF) Rig," *11th European Turbomachinery Conference 2015*, Madrid, Spain, 2015, pp. ETC–11–256.

[24] Meyer, R., Hakansson, S., Hage, W., and Enghardt, L., "Instantaneous flow field measurements in the interstage section between a fan and the outlet guiding vanes at different axial positions," *13th European Conference on Turbomachinery Fluid Dynamics & Thermodynamics 2019*, Madrid, Spain, 2019, pp. ETC2019–330. doi:https://doi.org/10.29008/ETC2019-330.

[25] Tapken, U., Gutsche, D., and Enghardt, L., "Radial mode analysis of broadband noise in flow ducts using a combined axial and azimuthal sensor array," *20th AIAA/CEAS Aeroacoustics Conference*, 2014. doi:10.2514/6.2014-3318.

[26] Caldas, L., Kruck, S., Klähn, L., Rudolphi, A., Meyer, R., Enghardt, L., and Tapken, U., "Construction and Assessment of an Inflow-Control-Device for a Low-Speed Aeroacoustic Fan Rig," *AIAA Journal*, Vol. 0, No. 0, 2022, pp. 1–14. doi:10.2514/1.J061729.

[27] Vinz, A., and Raichle, A., "Investigation of the effects of boundary layer ingestion engine integration on aircraft thrust requirement," *CEAS Aeronautical Journal*, 2024. doi:10.1007/s13272-024-00722-0.

[28] Caldas, L., Kissner, C., Behn, M., Tapken, U., and Meyer, R., "Comparison of Techniques for the Estimation of Flow Parameters of Fan Inflow Turbulence from Noisy Hot-Wire Data," *Fluids*, Vol. 6, No. 11, 2021. doi:10.3390/fluids6110372.

[29] Antoni, J., "Cyclostationarity by examples," *Mechanical Systems and Signal Processing*, Vol. 23, No. 4, 2009, pp. 987–1036. doi:10.1016/j.ymssp.2008.10.010.

[30] Caldas, L., and Meyer, R., "New method to separate turbulence statistics of fan rotor wakes from background flow," *Experiments in Fluids*, Vol. 64, No. 2, 2023, p. 32. doi:10.1007/s00348-023-03576-0.

[31] Tapken, U., Behn, M., Spitalny, M., and Pardowitz, B., "Radial mode breakdown of the ACAT1 fan broadband noise generation in the bypass duct using a sparse sensor array," *25th AIAA/CEAS Aeroacoustics Conference*, American Institute of Aeronautics and Astronautics, Reston, Virginia, 2019. doi:10.2514/6.2019-2525.

[32] Morfey, C. L., "Sound transmission and generation in ducts with flow," *Journal of Sound and Vibration*, Vol. 14, No. 1, 1971, pp. 37 – 55. doi:10.1016/0022-460X(71)90506-2.

[33] Tapken, U., "Analyse und Synthese akustischer Interaktionsmoden von Turbomaschinen," Dissertation, Technische Universität Berlin, Berlin, Deutschland, 2016.

[34] Staggat, M., "Modellierung und Prognose des Grenzschicht-Rotor-Interaktionsschalls für integrierte Triebwerke," Ph.D. thesis, Technische Universit"at Berlin, 2021.

[35] Moreau, A., "A unified analytical approach for the acoustic conceptual design of fans of modern aero-engines," Ph.D. thesis, Technical University Berlin, DLR research report DLR-FB-2017-56, 2017.

[36] Jenkins, G., "Models for the prediction of rear-arc and forward-arc fan broadband noise in turbofan engines," Ph. D. Thesis, University of Southampton, Southampton, UK, 2013. URL https://eprints.soton.ac.uk/361712/1/Gareth_Jenkins_PhD_Thesis.pdf.

[37] Liebeck, R., "Laminar separation bubbles and airfoil design at low Reynolds numbers," *10th Applied Aerodynamics Conference*, American Institute of Aeronautics and Astronautics, Reston, Virigina, 1992. doi:10.2514/6.1992-2735.

[38] Behn, M., Pilgrim, J., and Tapken, U., "Experimental validation of an analytical sound transmission model for fan stages," *30th AIAA/CEAS Aeroacoustics Conference*, Rome, Italy, 2024, pp. AIAA–2024–3290.

[39] Ganz, U. W., Joppa, P. D., Patten, T. J., and Scharpf, D. F., "Boeing 18-Inch Fan Rig Broadband Noise Test," , 1998. URL https://ntrs.nasa.gov/citations/19980236567.

[40] Klähn, L., Moreau, A., Caldas, L., Jaron, R., and Tapken, U., "Advanced analysis of fan noise measurements supported by theoretical source models," *International Journal of Aeroacoustics*, Vol. 21, No. 3-4, 2022, pp. 239–259. doi:10.1177/1475472X221093703.

[41] Moreau, S., Roger, M., and Christophe, J., "Flow Features and Self-Noise of Airfoils Near Stall or in Stall," *15th AIAA/CEAS Aeroacoustics Conference (30th AIAA Aeroacoustics Conference)*, American Institute of Aeronautics and Astronautics, Reston, Virigina, 2009. doi:10.2514/6.2009-3198.

[42] Fukano, T., and Jang, C.-M., "Tip clearance noise of axial flow fans operating at design and off-design condition," *Journal of Sound and Vibration*, Vol. 275, No. 3-5, 2004, pp. 1027–1050. doi:10.1016/S0022-460X(03)00815-0.